Detectability of standing accretion shock instabilities activity in supernova neutrino signals

Zidu Lin[1], Cecilia Lunardini,[1] Michele Zanolin,[2] Kei Kotake,[3] and Colter Richardson[2]

[1]*Department of Physics, Arizona State University, 450 E. Tyler Mall, Tempe, Arizona 85287-1504, USA*
[2]*Embry-Riddle Aeronautical University, Prescott, Arizona 86301, USA*
[3]*Department of Applied Physics & Research Institute of Stellar Explosive Phenomena, Fukuoka University, 8-19-1, Nanakuma, Fukuoka 814-0180, Japan*

We introduce a novel methodology for establishing the presence of standing accretion shock instabilities (SASI) in the dynamics of a core collapse supernova from the observed neutrino event rate at water- or ice-based neutrino detectors. The methodology uses a likelihood ratio in the frequency domain as a test-statistics; it is also employed to assess the potential to estimate the frequency and the amplitude of the SASI modulations of the neutrino signal. The parameter estimation errors are consistent with the minimum possible errors as evaluated from the inverse of the Fisher information matrix, and close to the theoretical minimum for the SASI amplitude. Using results from a core-collapse simulation of a 15 solar-mass star by Kuroda *et al.* [Astrophys. J. **851**, 62 (2017).] as a test bed for the method, we find that SASI can be identified with high confidence for a distance to the supernova of up to ∼6 kpc for IceCube and up to ∼3 kpc for a 0.4 Mt mass water Cherenkov detector. This methodology will aid the investigation of a future galactic supernova.

I. INTRODUCTION

The numerical study of the dynamics of core-collapse supernovae allowed in the recent decades to identify specific hydrodynamics mechanisms which control the evolution of the shock wave. Among these dynamics, one that is expected to produce signatures both in the neutrino luminosity and the gravitational wave emission is the standing accretion shock instability (SASI) [1,2]. SASI is a hydrodynamical mode with a typical frequency, phase and possibly varying amplitude that develops when a deformed stalled shock front precesses around the newly formed protoneutron star (PNS). Such precession in turn induces an asymmetric accretion onto the PNS, resulting in fluctuations in the luminosity of the emitted neutrinos, and the emission of gravitational waves (GW) (see, e.g., [3–6] and references therein).

Indications of SASI were first identified in two-dimensional (2D) numerical simulations [1,6–11], and then confirmed by three-dimensional (3D) simulations as well [12–18]. The precession frequency (and therefore the frequency of the neutrino modulations) was found to be between a few tens of Hz and 200 Hz [4,18–20] depending on the progenitor mass, nuclear equation of state (EOS), and progenitor rotation. A possible correlation of the SASI-modulated neutrino and GW signals has been studied in [4], which also demonstrated that a GW SASI signature could be contaminated by other effects (e.g., neutrino-driven convection and the associated turbulence). A multimessenger analysis joint with neutrinos, which could clarify the presence of SASI in GW, is particularly motivated.

While the frequency of the SASI is expected to be mostly related to the mechanical properties of the PNS, the duration of SASI signatures in neutrinos and GW reflects the duration of the phase when the shock wave is stalled, before either being launched to drive an explosion, or dying out so the star implodes directly into a black hole (failed supernova). Indeed, progenitors at the interface of the successful and failed explosions tend to exhibit longer periods with SASI [18].

At this moment, SASI is a hypothesis—supported by numerical simulations—that awaits observational tests. Neutrinos and GW are the only messengers that can, for a future galactic supernova, directly probe this phenomenon and provide measurements the relevant parameters (such as the SASI frequency and amplitude). Such measurements will clarify the properties of the PNS, the nuclear EOS, ultimately the yet-uncertain supernova explosion mechanism. The phase difference between GW and neutrino luminosity observed at Earth could also in principle (for an uncertainty-free signal at the source) probe propagation effects, like the time delay due to the neutrinos being massive [21,22]. It also carries the potential to estimate the different depths of the main production zone of neutrinos (the neutrinosphere) and of GW [4].

The theme of this paper is the detectability of SASI signatures in the neutrino luminosity as recorded at

neutrino detectors on Earth, and the potential of estimation of its main phenomenological parameters. The SASI-induced modulation of neutrino emission has been studied previously on the base of both two-dimensional [23,24] and three-dimensional [15,25] SASI-dominated supernova simulations. The neutrino signal in terms of its Fourier power spectrum was analyzed [18,19,21,26,27] in order to assess the detectability of SASI activity. The minimum requirement for signal detection was established by stating that the power spectrum of signal has to exceed the one of the background [19,21,26,28].

In this work we advance the topic to a more quantitative level, by establishing a framework which is new in the context of neutrino data analyses. This methodology is an implementation of the maximum likelihood principle, and uses the probability distribution of the observed power at different frequencies. As part of the likelihood-based analysis we also address the question of parameter estimation, and compare the results for the parameter variances to the optimally possible variance according to a Fisher matrix analysis of the problem.

The present paper is intended as a first step toward a joint description of the problem for neutrinos and GW, which is left for future work.

The paper is structured as follows. In Sec. II, generalities are given on SASI and on neutrino detection. In Sec. III, our methodology to establish the presence of SASI in a neutrino signal is presented, and results are shown using a specific numerical simulation as a test-bed of the method. Parameter estimation is then addressed in Sec. IV, and a discussion follows in Sec. V. Three appendices offer proofs and technical details to the interested reader.

II. GENERALITIES

A. Supernova neutrino detection

We consider neutrino detections in two different experimental settings. The first is a water Cherenkov detector at the Megaton mass scale, like the planned Hyper-Kamiokande (Hyper-K from here on) [29]. For simplicity, only the main detection channel, inverse beta decay $(\bar{\nu}_e + p \to n + e^+)$, is included here. Individual positrons are detected via their Cherenkov photon signature with high efficiency and excellent time resolution (microseconds or less [29]). Therefore, here an "event" from a supernova burst indicates an individual neutrino interacting within the volume of the detector. Background events due to other neutrino sources, cosmic rays or detector impurities—which in principle could mimic supernova neutrinos events—are negligible for a galactic supernova [30].

The number of supernova neutrino events in the detector is directly proportional to the number of target particles in the detector (and therefore to its mass), and it scales like the neutrino number flux, i.e., proportionally to D^{-2}, with D being the distance to the star. As a reference, here the expected Hyper-K mass of 0.44 Mt and 100% detector efficiency will be used; results for different detector masses can thus be obtained by rescaling D. Given the microsecond recording time scale, the number of events n_i in each millisecond time bin $[t_i, t_i + \Delta t]$ is subject to Poisson statistical fluctuations (standard deviation $\sigma_i = \sqrt{n_i}$), with negligible correlations between different time bins.

The second experimental setting refers to the kilometer-scale antarctic detector IceCube [31]. There, the detection concept is designed for multi-TeV neutrinos, and is based on digital optical modules (DOMs) positioned in geometrically sparse arrays in the antarctic ice. For a flux of ~10 MeV supernova neutrinos, individual neutrino interactions (mostly from inverse beta decay, like in water) cannot be resolved, however a surge of total photon count rate in the optical modules can be observed as a signal. In this context, an event is intended to be the observation of a photon in a DOM.

In contrast with Hyper-K, in IceCube the background level is relatively high, at a rate of $\dot{n} \simeq 1340$ ms^{-1} [21,32]. Therefore, the number events n_i in each time bin is the number of photons recorded in the entire detector in that time bin, and is the sum of the contributions of the supernova signal (scaling like D^{-2}) and of background (fixed, and constant in time). Note that in this work we focus on the dominant emission signatures of electron antineutrinos (in both IceCube and Hyper-K), and we shall leave the consideration of multiflavor interactions (albeit important, see an in-depth review by Mirizzi *et al.* [3]) for future work.

B. SASI: Physics and numerical predictions

We use the numerically calculated neutrino event rates for IceCube and Hyper-K from a 3D general relativistic (GR) simulation (model SFHx, where SFHx indicates the equation of state by [33]) by Kuroda, Kotake, Hayama and Takiwaki (KKHT from here on) [4] as a test bed of a realistic scenario where SASI effects are present in the neutrino luminosity. They are shown in Fig. 1. For simplicity, the observer's direction is taken along the polar (e.g., the z) axis of the source as a fiducial case, where the flux-projection effects and the detection efficiencies for estimating the event rates are taken into account following Tamborra *et al.* [28].

In the KKHT model, the 3D hydrodynamics evolution is self-consistently followed from the onset of core-collapse of a 15 $M_\odot$ star [34], through core bounce, up to ~350 ms after bounce. As consistent with the outcomes from recent 3D models (e.g., [5,15,35]), the hydrodynamic evolution is characterized by the prompt convection phase shortly after bounce ($T_{pb} \lesssim 20$ ms with T_{pb} the postbounce time), then the linear (or quiescent) phase ($20 \lesssim T_{pb} \lesssim 140$ ms), which is followed by the nonlinear phase when the vigorous activity of SASI was observed for the model. The dominance of the SASI over neutrino-driven convection persists
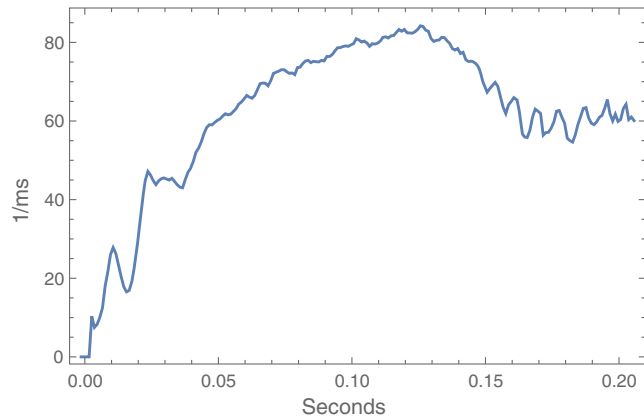
FIG. 1. Predicted neutrino event rate at Hyper-K from the KKHT model of a 15 $M_\odot$ progenitor with the SFHx equation of state [4], for a star at distance $D = 10$ kpc.

over $140 \lesssim T_{pb} \lesssim 300$ ms, after which neutrino-driven convection dominates over the SASI (see [36] for more details). In [36], the SASI frequency was roughly estimated as $\dot{M}/M \sim 100$ Hz, where $M \sim 10^{-3}$ $M_\odot$ and $\dot{M} \sim 0.1$ $M_\odot/\text{s}$ denote the typical mass and mass accretion rate

in the gain region, respectively, which is consistent with the numerically obtained SASI-modulated neutrino frequency (e.g., Fig. 7 of [4]).

In the simulation, the Baumgarte-Shibata-Shapiro-Nakamura formalism was employed to evolve the metric [37,38], and the GR neutrino transport was solved by an energy-integrated M1 scheme [39]. For simplicity, effects of neutrino flavor oscillations (e.g., the Mikheyev-Smirnov-Wolfenstein (MSW) effect [40], and collective neutrino oscillations, see [3] and references therein for a review) are neglected in this study (see, e.g., [19] for a brief discussion of the validity of this approximation).

Here the supernova burst simulated by KKHT will be used as representative of a future SASI-carrying signal in the two detectors of interest. It will be compared with a similar signal that has no SASI features in it. Such null model is constructed by smoothing out the SASI oscillations from the original KKHT model. The smoothing is done by taking the event rates averaged over eight time bins, each of 1 ms width, and performing a polynomial interpolation of these averaged rates. A zoomed-in plot of the KKHT and smoothed out rates is given in Fig. 2 (black solid lines in left panes).
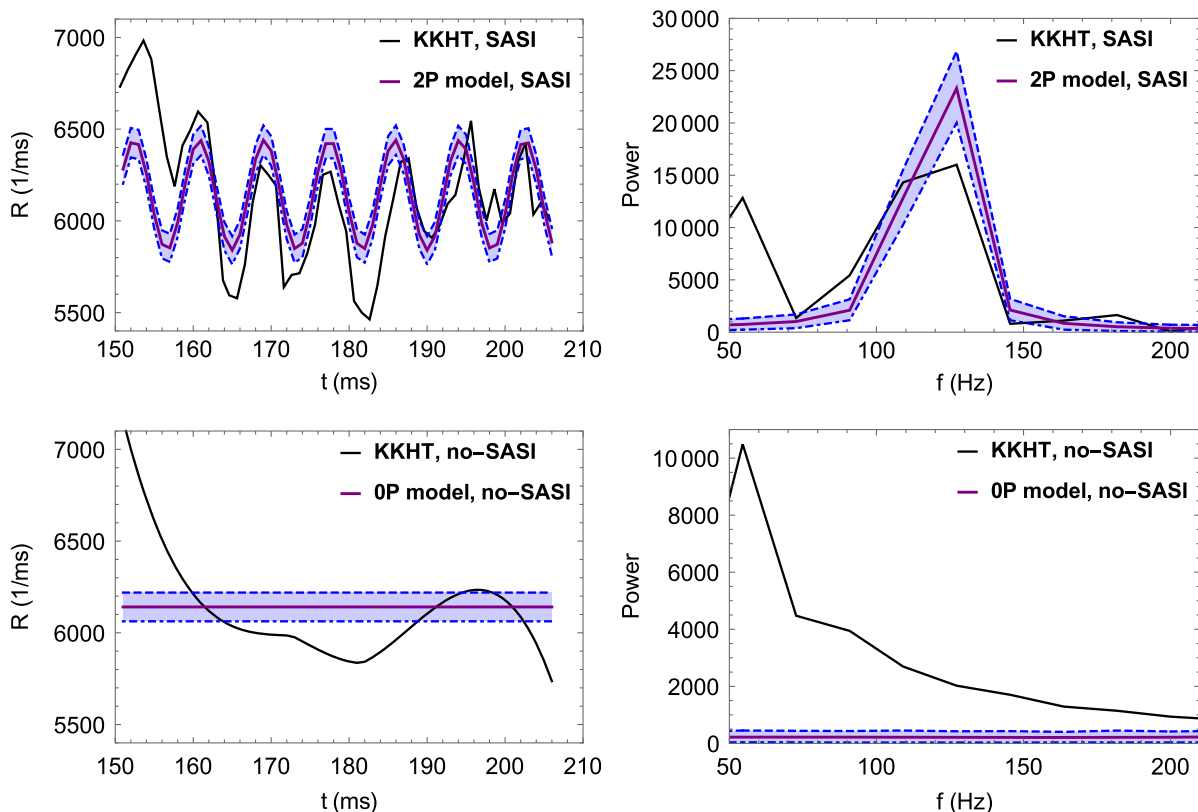

FIG. 2. Neutrino event rate (left panels) and its power spectrum (right panels) at Hyper-K for distance $D = 1$ kpc. Shown as solid black lines are a case where there is SASI (upper panes, from the KKHT model), and no SASI (lower panes, derived from the KKHT model with smoothing, see text). We also show (solid, purple curves) the predictions of the 2-parameter template [2P, Eq. (1)] and of the 0-parameter template [0P, Eq. (2)], for estimated best-fitting parameters ($f_S = 119.72$ Hz, $a = 0.049$ and $A = 6141.54$, see Eq. (1) and Table I). The shaded (blue) bands characterize the probability density distributions with the width of one standard deviation.

III. TESTING FOR SASI: LIKELIHOOD RATIO METHOD

In this section, we set up the formalism necessary to our statistical method. Considering the oscillatory character of the SASI signatures, we choose to work in the frequency space, and establish the discretized power spectrum of the neutrino time profile as the observable of interest. The statistical behavior of the power spectrum is then presented. Finally, the likelihood ratio as test-statistics is defined and used to assess the detectability of the SASI. We use the likelihood ratio as deciding statistic for the hypothesis test because of its optimality properties, which are described by the Neymann-Pearson Lemma [41]. For clarity, in what follows the symbols with tilde (e.g., $\tilde{N}$) will indicate an actual outcome of a measurement, which is affected by statistical fluctuations. The same symbol without tilde (e.g., N) will be used for the mean, "true" value of the same quantity.

A. Neutrino time profile templates

When data from a supernova burst are analyzed, it can be useful—as it is often done in neutrino data analyses, see, e.g., [21]—to fit the event rate time profile with simplified analytical templates that, while necessarily inaccurate, will allow to gain analytical understanding and to estimate the main phenomenological parameters. The latter can then be compared with predictions of detailed numerical simulations for greater insights into the microphysics at play. In this work, we use two parametric templates which characterize the main features of neutrino signals with and without the SASI activity respectively, to study the potential of a data analysis algorithm to identify the presence of SASI.

For the case with SASI activity we choose a single frequency function:

$$R_2(t) = (A - n)(1 + a \sin(2\pi f_S t)) + n, \qquad (1)$$

where A is the time-averaged event rate (the "DC component") in the detector including instrumental noise (after possible experimental cuts), a is the relative SASI amplitude, n is the mean value of the background rate ($n = 0$ for Hyper-K), and f_S is the nominal frequency of the SASI. The second template, for the case without SASI, is a constant:

$$R_0(t) = A, \qquad (2)$$

[with A having the same meaning as in Eq. (1)].

In our method, only f_S and a will be treated as free parameters with respect to which the likelihood will be maximized. We assume that other relevant quantities, such as the DC component, A, and the starting time (t_0) and duration (τ) of the SASI activity, can be determined

separately, by using theoretical priors, visual inspection, or a separate algorithm. For A, it is immediate to see that it can be measured with high precision (i.e., negligible uncertainty), without the need of a fit. Its relative uncertainty is $\delta A/A = 1/\sqrt{N_{ev}} \ll 1$ where N_{ev} is the total number of events, and $N_{ev} \gtrsim 2500$ in all the cases examined here (we also assume that systematic uncertainties on n are negligible, because background rates can be measured precisely over years of data-taking).

With regard to t_0 and τ, here they are fixed to be $t_0 = 155$ ms post-bounce, and $\tau = 55$ ms, consistently with the KKHT simulation results (Fig. 1). Fixing these quantities is legitimate in the spirit of answering the question whether there is indication of single-frequency fluctuations in a signal between two chosen (generic) instants of time. Realistically, in the context of a more specific search for SASI effects, t_0 and τ could be at first set using rough estimations from visual inspections of the data, in conjunction with expectations from the theory. Indeed, a delay in the onset of SASI (relative to the bounce time) is expected considering that SASI requires the shockwave to come to a stalling point. We checked that 3D numerical simulations roughly place t_0 in the interval ~ 0.1–0.4 s post-bounce [16,36,42–44], with τ being even more uncertain. It is possible that, by the time the next galactic supernova is observed, theoretical progress will be able to place stronger priors on t_0 and τ. The method proposed here will be applicable to data with externally-estimated (not optimized) t_0 and τ; the lack of optimization of these parameters will result in certain loss of power of the method, which can be overcome by generalizing the method to include τ and t_0 as fit parameters.

B. Time series and power spectrum

Let us consider the events that are recorded in a detector after an initial time t_0, in time bins of width $\Delta = 1$ ms. The jth time bin then corresponds to the time $t_j = t_0 + j\Delta$. The observed number of events in the same bin will then be $\tilde{N}(t_j)$, which is a random variable fluctuating around its mean $N(t_j) \simeq R(t_j)\Delta$.

Following [21,26], we perform a discrete Fourier transform of the time series $\{\tilde{N}(t_j)\}$ over the time interval $[t_0, t_0 + \tau]$, containing $N_{\text{bins}} = \tau/\Delta$ time bins. The discrete frequency resolution is then:

$$\delta = \frac{1}{\tau}, \qquad (3)$$

which represents the minimum width of frequency bins for which statistical independence between adjacent bins can be realized (see the discussion in Appendix A). For our fiducial value $\tau = 55$ ms, the resolution is $\delta = 18$ Hz [45]. The Nyquist frequency becomes [41]

$$f_{Nyq} = \frac{1}{2\Delta}, \tag{4}$$

which corresponds to the frequency index

$$k_{Nyq} = \frac{f_{Nyq}}{\delta} = \frac{\tau}{2\Delta} = \frac{1}{2} N_{\text{bins}}. \tag{5}$$

We define the discrete Fourier-transformed neutrino signal as:

$$\tilde{h}(k\delta) = \sum_{j=0}^{N_{\text{bins}}-1} \tilde{N}(t_j) e^{i2\pi j \Delta k\delta}, \tag{6}$$

and the one-sided power spectrum, similarly to [41] as:

$$\tilde{P}(k\delta) = \begin{cases} 2|\tilde{h}(k\delta)|^2/N_{\text{bins}}^2 & \text{for } 0 < k\delta < f_{Nyq}, \\ |\tilde{h}(k\delta)|^2/N_{\text{bins}}^2 & \text{for } k\delta = 0 \end{cases} \tag{7}$$

(here the identity $(|\tilde{h}(k\delta)|^2 + |\tilde{h}(-k\delta)|^2) = 2|\tilde{h}(k\delta)|$ was used).

The factor of $1/N_{\text{bins}}^2$ is included in order to fix the normalization, so that at $k=0$ we have $\tilde{P}(0) = (\tilde{N}_{ev}/N_{\text{bins}})^2$ [here $\tilde{N}_{ev} = \sum_{j=0}^{N_{\text{bins}}-1} \tilde{N}(t_j)$].

Figure 2 shows an illustration of the discretized time profile, and the corresponding power spectra, for the KKHT model, with and without SASI [as well as for the two templates in Eqs. (1) and (2)]. For the latter, the parameters have been fit to maximize the likelihood (see Eq. (10) in the following section) to best reproduce the general features of the neutrino event rates predicted by the KKHT model. The figure shows that, qualitatively, the templates capture the main features of the realistic, numerically calculated time and frequency profiles. An exception is the peak at $f \sim 60$ Hz in the power spectrum of the no-SASI model, which is not reproduced by the template. We checked that this peak is due to the "wavy" structure at $t \sim 180$–200 ms in the numerical model.

C. The SASI-meter

Let us now consider the series of power spectrum values at the discrete frequencies $k\delta$, $P(k\delta)$, and their statistical properties. Considering that (i) the probability that a single neutrino interacts in the detector is very small, (ii) event counts in different time bins are statistically independent (see Sec. II), and (iii) $N(t_j) \gtrsim 10$ (large number approximation), we conclude that the binomial distribution for $N(t_j)$ approaches a Gaussian distribution with a variance proportional to the square root of the mean number (Poisson process): $s^2(t_j) = N(t_j)$. This implies (see the proofs in Appendices A and B) that the real part and imaginary part of the discrete Fourier transform, $h(k\delta)$ [Eq. (6)], are also Gaussian-distributed, and the probability distribution of the power spectrum $\tilde{P}$ at a given frequency is given by

$$\text{Prob}(\tilde{P}) = \frac{N_{\text{bins}}^2}{4\sigma^2} \exp\left[-\frac{N_{\text{bins}}^2}{4\sigma^2}(\tilde{P} + P)\right]$$
$$\times I_0\left(\frac{N_{\text{bins}}^2}{2\sigma^2}\sqrt{\tilde{P}P}\right), \tag{8}$$

where I_0 is the modified Bessel function of the first kind, and

$$\sigma^2 = \frac{N_{ev}}{2}. \tag{9}$$

The object of this study is to perform a hypothesis test for the presence of SASI. There is evidence from numerical simulations that the SASI only develops within a certain range of frequencies from a few tens of Hz to about 250 Hz [5,25,36,46–48]. Therefore, we apply a frequency cut, and restrict the analysis to the interval from 54 Hz to 216 Hz. The corresponding range of wavenumbers is $k = 3, 4, 5, …, 12$. In addition to being motivated by estimates of the SASI frequency, the cut is instrumental to exclude a large peak at low frequency due to the spectral leakage [41] from 0 Hz.

Let us now define the likelihood that a given observed power series vector, $\tilde{\mathcal{P}} = \{\tilde{\mathcal{P}}_k\}$ (i.e., the series of powers for discrete wavenumbers k) is a realization of a certain hypothesis, which can be described by a parametric template. It is defined as:

$$L(\tilde{\mathcal{P}}, \Omega) = \prod_{k=3}^{12} \text{Prob}(\tilde{\mathcal{P}}_k, P_k(\Omega)), \tag{10}$$

where $P_k(\Omega)$ is the power predicted by the template, and Ω indicates the set of parameters of the template.

Given two hypotheses (i.e., two templates) with parameters Ω and Ω_0, and a fixed observed set $\tilde{\mathcal{P}}$, the likelihood ratio is

$$\mathcal{L}(\tilde{\mathcal{P}}) = \frac{\text{Max}_{\Omega}[L(\tilde{\mathcal{P}}, \Omega)]}{\text{Max}_{\Omega_0}[L(\tilde{\mathcal{P}}, \Omega_0)]}. \tag{11}$$

In the numerator (denominator), the first (second) hypothesis is used and the likelihood is maximized with respect to the parameters Ω (Ω_0). In this work, the templates in Eqs. (1) and (2) will be used as representative of the SASI and no-SASI cases. Their parameters are $\Omega = \{a, f_S\}$ and $\Omega_0 = \{\text{Null}\}$ respectively.

It is intuitive to see how the likelihood ratio in Eq. (11) is sensitive to SASI. Since our templates R_2 [Eq. (1)] and R_0 [Eq. (2)] capture well the main features of the neutrino event rates of the models with and without SASI respectively, as the SASI features in the data become more pronounced, the numerator Eq. (11) is likely to increase (generally better fit for the R_2 template), while at the same time the denominator is likely to decrease (poorer fit for the R_0 template), so $\mathcal{L}$ is likely to increase. Vice-versa, $\mathcal{L}$ will
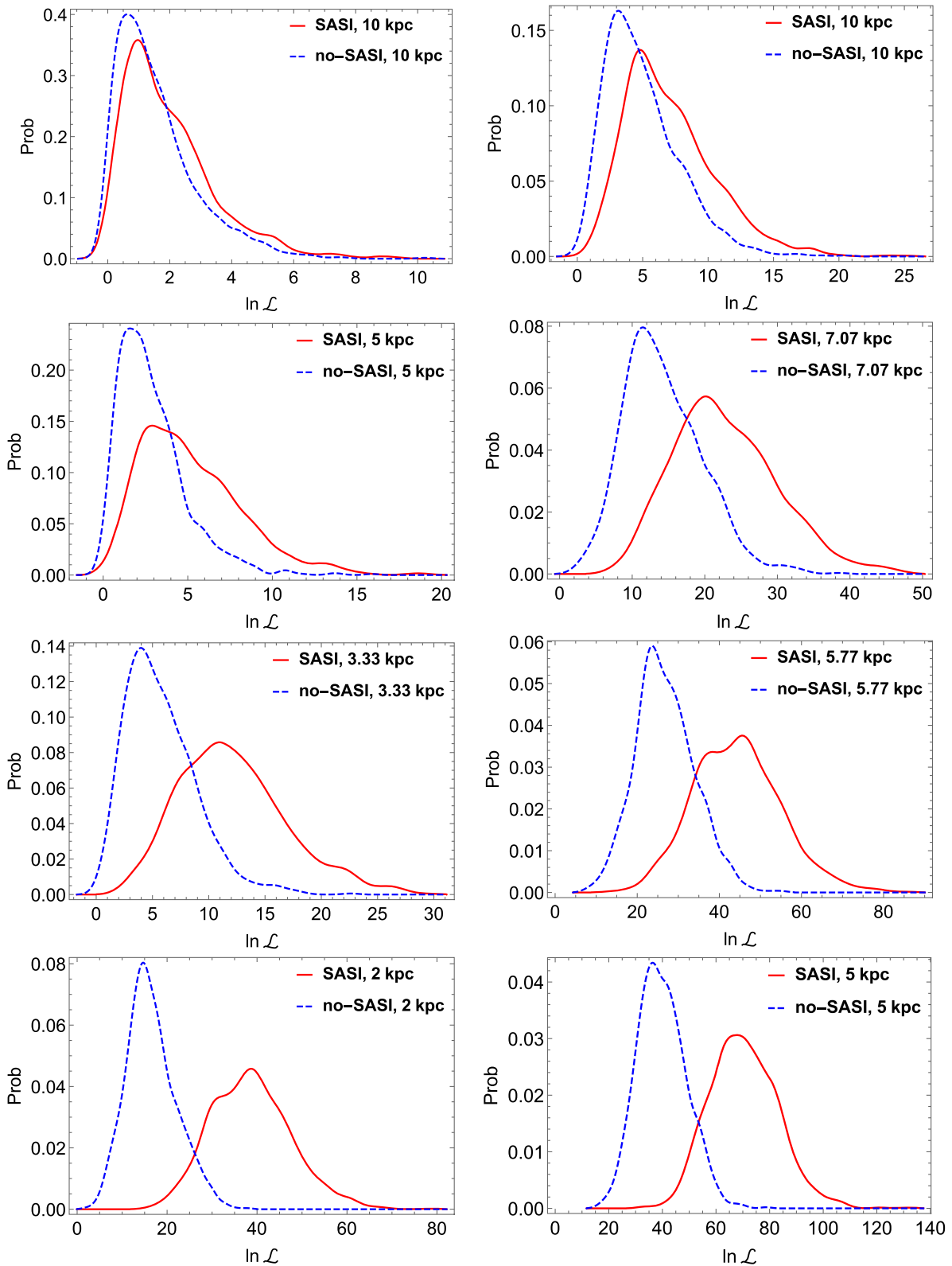
FIG. 3.   Likelihood ratio probability distribution for SASI and no SASI case in Hyper-K (left) and IceCube (right), for different values of the distance D to the star (chosen to correspond to integer increments of the number of events, see legends). The likelihoods have been obtained using simulated neutrino signal according to the KKHT model.

take lower values if the SASI signatures in the data become weaker. Therefore, Eq. (11) serves as our *"SASI-meter"* to identify the presence of SASI.

To assess the effectiveness of the SASI-meter quantitatively, we need to find the probability distributions of $\mathcal{L}$ (or, equivalently, $\ln \mathcal{L}$) under the two hypotheses. This was done by simulating (using a Monte Carlo method) $N_{st} = 10^3$ sets $\tilde{\mathcal{P}}$ using the KKHT model with and without SASI, so we will have $\mathcal{L}_S \equiv \mathcal{L}(\tilde{\mathcal{P}}_{SASI})$ and $\mathcal{L}_{nS} \equiv \mathcal{L}(\tilde{\mathcal{P}}_{no\text{-}SASI})$, and their probability density distributions, $\text{Prob}(\mathcal{L}_S) \simeq \text{Prob}(\mathcal{L}|S)$ (where $\text{Prob}(\mathcal{L}|S)$ indicates the "true" probability distribution, which would be obtained in the limit $N_{st} \to \infty$) and $\text{Prob}(\mathcal{L}_{nS}) \simeq \text{Prob}(\mathcal{L}|nS)$.

A useful way to describe these two distributions, and compare them with one another, is to examine the probabilities that—under the two hypotheses—the likelihood ratio exceeds a certain threshold value, Λ:

$$P_D = \int_{\mathcal{L}>\Lambda} \text{Prob}(\mathcal{L}|S)d\mathcal{L}, \tag{12}$$

$$P_{\text{FI}} = \int_{\mathcal{L}>\Lambda} \text{Prob}(\mathcal{L}|nS)d\mathcal{L}. \tag{13}$$

Λ usually represents a value of the likelihood ratio above which the SASI hypothesis is accepted as true ("detection"). Therefore, P_D takes the meaning of SASI *detection probability*, because it represents the probability that the method accepts the SASI hypothesis as true when the SASI is in fact true. P_{FI} then represents the *false identification probability*, i.e., the probability that the SASI hypothesis is accepted when in fact the no-SASI hypothesis is the true one.

The formalism discussed in this section becomes clearer in light of the results we have obtained, which are going to be illustrated next.

D. Results: SASI or no-SASI?

Our main results for hypothesis testing are summarized in Fig. 3, for Hyper-K and IceCube, and for different distances to the supernova. For each detector and distance, the figure shows the probability distributions of $\ln \mathcal{L}_S$ and $\ln \mathcal{L}_{nS}$.

We observe that, reflecting the expected sensitivity of our SASI-meter, for short distances the two distributions are widely separated, with the distribution for the SASI (no-SASI) case peaking at lower (higher) values of the likelihood ratio [49]. The separation means that, if the SASI hypothesis is true, there is a large probability that the measured value of $\ln \mathcal{L}$ will fall in a region where the no-SASI hypothesis is strongly disfavored [i.e., $\text{Prob}(\mathcal{L}|nS) \ll \text{Prob}(\mathcal{L}|S)$]. A similar argument holds if the no-SASI hypothesis is true. We conclude, then, that for a relatively close supernova ($D \sim$ few kpc) the two hypotheses are likely to be distinguished with high confidence.

The separation between the two probability distributions decreases as D increases, until, for $D \sim 10$ kpc, the SASI and no-SASI curves almost completely overlap, meaning that the two hypotheses are very unlikely to be distinguished. The dependence on the distance is due to how the size of the statistical fluctuations increases with D, eventually overpowering the SASI, which therefore becomes invisible.

The trends shown in Fig. 3 are reflected in the behavior of the detection and false identification probabilities, P_D and P_{FI} [Eqs. (12) and (13)]. These are described by the receiver operating characteristic curve (ROC). The ROC is defined as the curve described in a plane by the points $(P_{FI}(\Lambda), P_D(\Lambda))$, where Λ varies in the interval $[0, +\infty]$. Figure 4 shows the ROC for Hyper-K and IceCube for several distances from the star. The plots show the general features of the ROC: it passes by the points (0,0) and (1,1) [corresponding to $\Lambda \to +\infty$ and $\Lambda \to 0$ respectively, see Eqs. (12) and (13)]. Furthermore, the curve lies in the region $P_D > P_{FI}$, as expected from Fig. 3. A high detectability potential corresponds to a ROC where P_D is as close
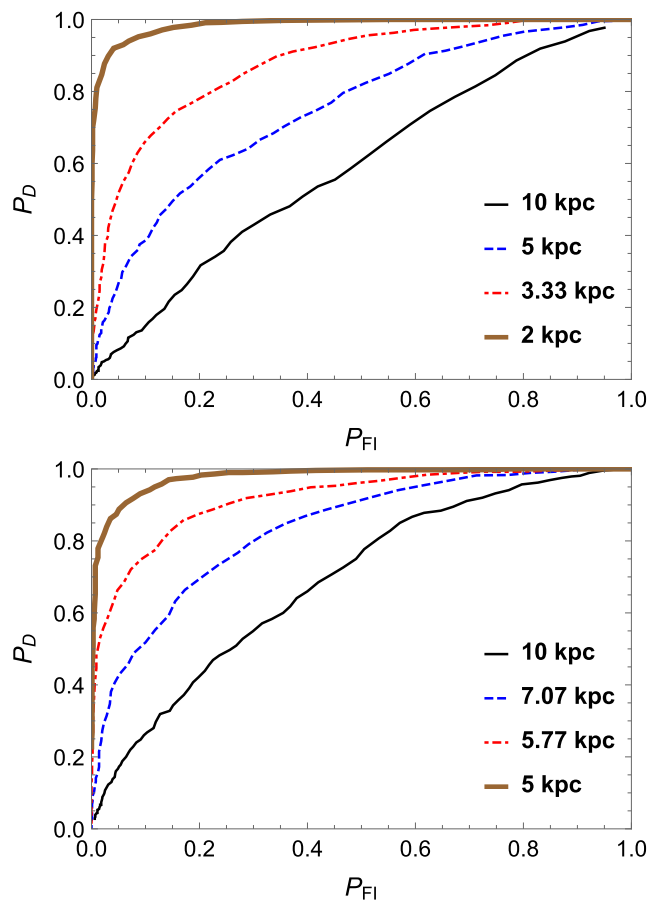

FIG. 4. Receiver operating characteristic curves based on KKHT model for Hyper-K (top panel) and Ice Cube (bottom panel), for several distances to the supernova. See Eqs. (12) and (13).

as possible to 1 and at the same time P_{FI} is as close as possible to 0. For example, for IceCube and $D = 5$ kpc, the ROC passes by the point $(P_{FI}, P_D) \simeq (0.1, 0.95)$, meaning that, if a 10% false identification rate is considered acceptable, the likelihood ratio will establish the presence of the SASI in 95% of the cases. The same situation is realized for Hyper-K for $D \simeq 2$ kpc. Naturally, the ROC deteriorates as D decreases, and ultimately (for $D \gtrsim 10$ kpc) it converges to the line $P_D = P_{FI}$, which corresponds to a neutrino signal with SASI being completely indistinguishable from a signal without SASI. The ROC curves allow to estimate the range where a fixed P_D is achieved for a desired P_{FI}. If, e.g., we require the ROC to have $P_D \geq 0.7$ for $P_{FI} = 0.1$, Fig. 4 indicates that the largest distance of sensitivity to the SASI is $D \simeq 6$ kpc for IceCube and $D \simeq 3$ kpc for Hyper-K.

IV. PARAMETER ESTIMATION

A. Likelihood ratio and best fit parameters

For the scenarios where the SASI hypothesis is accepted as true $(\mathcal{L} > \Lambda)$, the next step is estimation of the parameters. For definiteness, here we present results for Λ that corresponds to $P_{FI} = 0.1$ [Eq. (13)].

In our method, the best fit values of the SASI frequency, $\bar{f}_S$, and of the amplitude, $\bar{a}$, are found as the values that maximize the likelihood $L(\tilde{\mathcal{P}}, \Omega)$, within the process of constructing the likelihood ratio [Eq. (11)]. From that process, we obtained the probability distributions of $\bar{f}_S$, and $\bar{a}$. We then calculated the mean and standard deviation of $\bar{f}_S$ and $\bar{a}$. The standard deviation gives an estimate of approximately 68% confidence level error with which an estimate of a given parameter can be obtained.

The results are shown in Fig. 5 and Tables I (for Hyper-K) and II (for IceCube). For Hyper-K and $D = 10$ kpc, where the sensitivity to the SASI is poor, the distribution for $\bar{f}_S$ is very broad, with roughly all values being equally probable. This indicates that, although there might be indication of an oscillatory behavior in the data (such that the likelihood ratio is above the threshold), such outcome is most likely to be due to random statistical fluctuations and not to SASI. An estimate of the frequency would have a large error and might not be physically meaningful. The corresponding distribution for $\bar{a}$ is similarly broad for $\bar{a} \gtrsim 0.03$, indicating that, as long as there is indication of an oscillatory pattern in the data, its amplitude can vary widely, and is probably driven by statistical fluctuations.
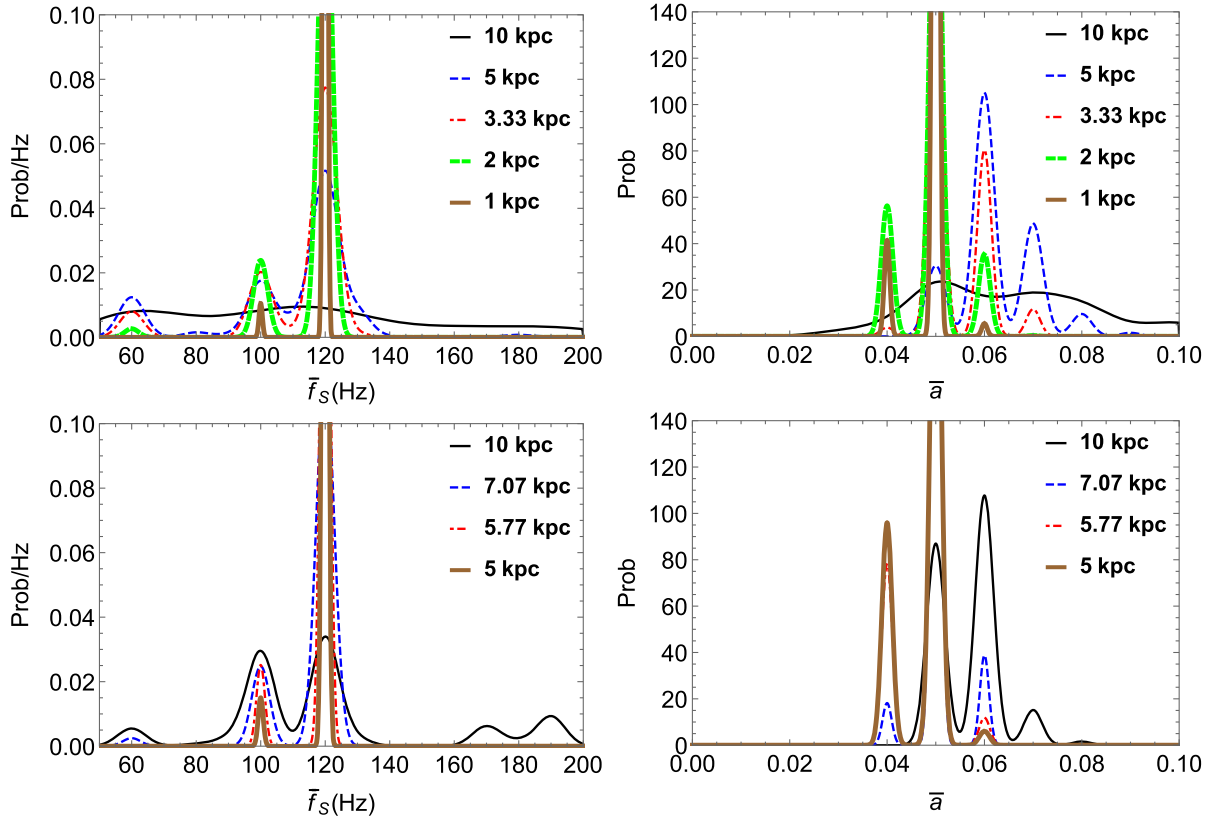

FIG. 5.   Probability distribution of the best-fit values of the SASI frequency, $\bar{f}_S$ (left), and oscillation amplitude, $\bar{a}$ (right), for Hyper-K (top) and for IceCube (bottom), for several distances to the supernova. Only cases with sufficient statistical indication of SASI activity are considered here, by imposing a threshold on the likelihood ratio (corresponding to $P_{FI} > 0.1$, see text). Here, the likelihoods have been obtained using simulated neutrino signal according to the KKHT model.

TABLE I. Mean and standard deviation of the parameter distributions in Fig. 5, for Hyper-K. The numbers in the parentheses are the Cramer-Rao lower bounds, calculated using Fisher matrix in the time domain. For larger D, where the selection effects on $\mathcal{L}$ are strong, a direct comparison is not meaningful and therefore the Cramer-Rao bounds are not shown.

SASI	10 kpc	5 kpc	3.33 kpc	2 kpc	1 kpc
f(Hz)	111.77	109.2	111.67	116.49	119.72
δf(Hz)	42.31	22.61	16.7	9.64(0.08)	2.35(0.04)
a	0.065	0.062	0.054	0.049	0.049
δa	0.017	0.008	0.0059	0.0053(0.0047)	0.0026(0.0023)

As D decreases ($D \lesssim 5$ kpc or so) the distributions of both $\bar{f}_S$ and $\bar{a}$ start to concentrate around the physical values of the injected SASI model, $\bar{f}_S \sim 120$ Hz and $\bar{a} \sim 0.05$, indicating a sensitivity to the physical SASI signal above statistical fluctuations. This trend appears in Table I as well, where one can see the decrease of the standard deviation with the decreasing distance. We note that the width of the distributions for a and f_S depend in part on how the time structure of the neutrino signal in the KKHT model is only roughly reproduced by the simplified template, Eq. (1). As a consistency test, we checked that using simulated data drawn from the simplified template has the (expected) effect of producing narrower parameter distributions [50].

We caution the reader about the meaning of the multiple peaks that appear in the distributions in Fig. 5: these peaks reflect the discrete structure of the power spectrum series $\{\tilde{P}_k\}$ which is being analyzed, which has a resolution (frequency bin size) of about 20 Hz (see Eq. (3) and Fig. 2), and therefore do not have a direct physical meaning.

The probability distributions and tabulated values (Table II) for IceCube show a structure and dependence on D similar to those for Hyper-K. A difference is that at $D = 10$ kpc, the sensitivity to SASI is not completely washed out by the statistical fluctuations, so it might be possible to obtain a (coarse) measurement of f_S.

B. Fisher information matrix and minimum uncertainties

In this section we aim at comparing the standard deviations of the SASI parameters obtained using the

TABLE II. Mean and standard deviation of the parameter distributions in Fig. 5, for IceCube. The numbers in the parentheses are the Cramer-Rao lower bounds, calculated using Fisher matrix in the time domain. For larger D, where the selection effects on $\mathcal{L}$ are strong, a direct comparison is not meaningful and therefore the Cramer-Rao bounds are not shown.

SASI	10 kpc	7.07 kpc	5.77 kpc	5 kpc
f(Hz)	120.45	115.57	118.33	119.43
δf(Hz)	33.36	10.85	5.53 (0.078)	3.34 (0.063)
a	0.057	0.050	0.048	0.048
δa	0.0064	0.0036	0.0047(0.0041)	0.0046 (0.0034)

likelihood ratio method with the theoretical lower bound in the accuracy. The latter is given by the Cramer-Rao lower bound [41], and is derived from the Fisher information matrix (FIM). We begin by summarizing the main formulas of the FIM formalism; these will then be applied to the case at hand.

Let us consider a generic template $R(t_i)$ for the event rate at discrete times, t_i ($i = 1, 2, …, N$), which depends on a set of parameters, θ_α ($\alpha = 1, 2, 3, …, K$) (note that, for our choice of unitary bin size, $\Delta = 1$ ms, the event rate and the number of events are numerically the same. Here we omit the factor Δ to keep the notation compact). The FIM is a $K \times K$ matrix, found from the probability distribution. We define the joint probability as:

$$\text{Prob}(\tilde{R}) = \prod_{i=0}^{N} \text{Prob}(\tilde{R}_i), \qquad (14)$$

where $\tilde{R}$ is the series of observed neutrino rate $\{\tilde{R}(t_1), \tilde{R}(t_2), …\tilde{R}(t_N)\}$ in time domain. The FIM describes how much each parameter affects the distribution via its second derivatives:

$$\Gamma_{\alpha\beta} = \left\langle -\frac{\partial^2 \ln \text{Prob}(\vec{R})}{\partial \theta_\alpha \partial \theta_\beta} \right\rangle, \qquad (15)$$

In the assumption that $\text{Prob}(\tilde{R}(t_i))$ is a multivariate Gaussian distribution in the time domain, the FIM reduces to the following expression (see Appendix C):

$$\Gamma_{\alpha\beta} = \mu_\alpha^T \Sigma^{-1} \mu_\beta + \frac{1}{2} \text{Tr}[\tilde{c}_\alpha \tilde{c}_\beta], \qquad (16)$$

where μ_α^T and μ_β are N-dimensional vectors (one component for each value of t_i), defined as:

$$\mu_\alpha = \frac{\partial \tilde{R}}{\partial \theta_\alpha}, \qquad (17)$$

and Σ^{-1} is the inverse of the $N \times N$ diagonal covariance matrix:

$$\Sigma^{-1} = \begin{bmatrix} R(t_1)^{-1} & 0 & 0 & 0 & 0 \\ 0 & R(t_2)^{-1} & 0 & 0 & 0 \\ 0 & 0 & R(t_3)^{-1} & 0 & 0 \\ 0 & 0 & 0 & \ddots & 0 \\ 0 & 0 & 0 & 0 & R(t_N)^{-1} \end{bmatrix}. \qquad (18)$$

Finally $\tilde{c}_\alpha$ is defined as the inverse of the covariance matrix times the partial derivative of the matrix:

$$\tilde{c}_\alpha = \Sigma^{-1} \frac{\partial \Sigma}{\partial \theta_\alpha}. \tag{19}$$

The Cramer-Rao bound on a parameter θ_α is given by:

$$\delta\theta_\alpha \geq \sqrt{(\Gamma^{-1})_{\alpha\alpha}} \tag{20}$$

We can now specialize the FIM formalism to our case, where the template is the one in Eq. (1), and we have two parameters, $\theta_1 = a$ and $\theta_2 = f_S$. Therefore:

$$R(t_i) = R_2(t_i) = (A-n)(1+a\sin(2\pi f_s t_i)) + n \tag{21}$$

$$\mu_1 = (A-n)\sin(2\pi f_s t_i) \tag{22}$$

$$\mu_2 = 2\pi t_i(A-n)a\cos(2\pi f_s t_i). \tag{23}$$

The elements of the Fisher matrix in time domain can be written analytically as below:

$$\Gamma_{11} = \sum_{i=1}^{N} \frac{(A-n)^2 \sin(2\pi f_s t_i))^2}{(A-n)(1+a\sin(2\pi f_s t_i)) + n}$$
$$+ \frac{(A-n)^2 \sin(2\pi f_s t_i))^2}{2((A-n)(1+a\sin(2\pi f_s t_i)) + n)^2}, \tag{24}$$

$$\Gamma_{12} = \sum_{i=1}^{N} \frac{2a(A-n)^2\pi t_i \sin(2\pi f_s t_i)\cos(2\pi f_s t_i)}{(A-n)(1+a\sin(2\pi f_s t_i)) + n}$$
$$+ \frac{a(A-n)^2\pi t_i \sin(2\pi f_s t_i)\cos(2\pi f_s t_i)}{((A-n)(1+a\sin(2\pi f_s t_i)) + n)^2}, \tag{25}$$

$$\Gamma_{21} = \sum_{i=1}^{N} \frac{2a(A-n)^2\pi t_i \sin(2\pi f_s t_i)\cos(2\pi f_s t_i)}{(A-n)(1+a\sin(2\pi f_s t_i)) + n}$$
$$+ \frac{a(A-n)^2\pi t_i \sin(2\pi f_s t_i)\cos(2\pi f_s t_i)}{((A-n)(1+a\sin(2\pi f_s t_i)) + n)^2}, \tag{26}$$
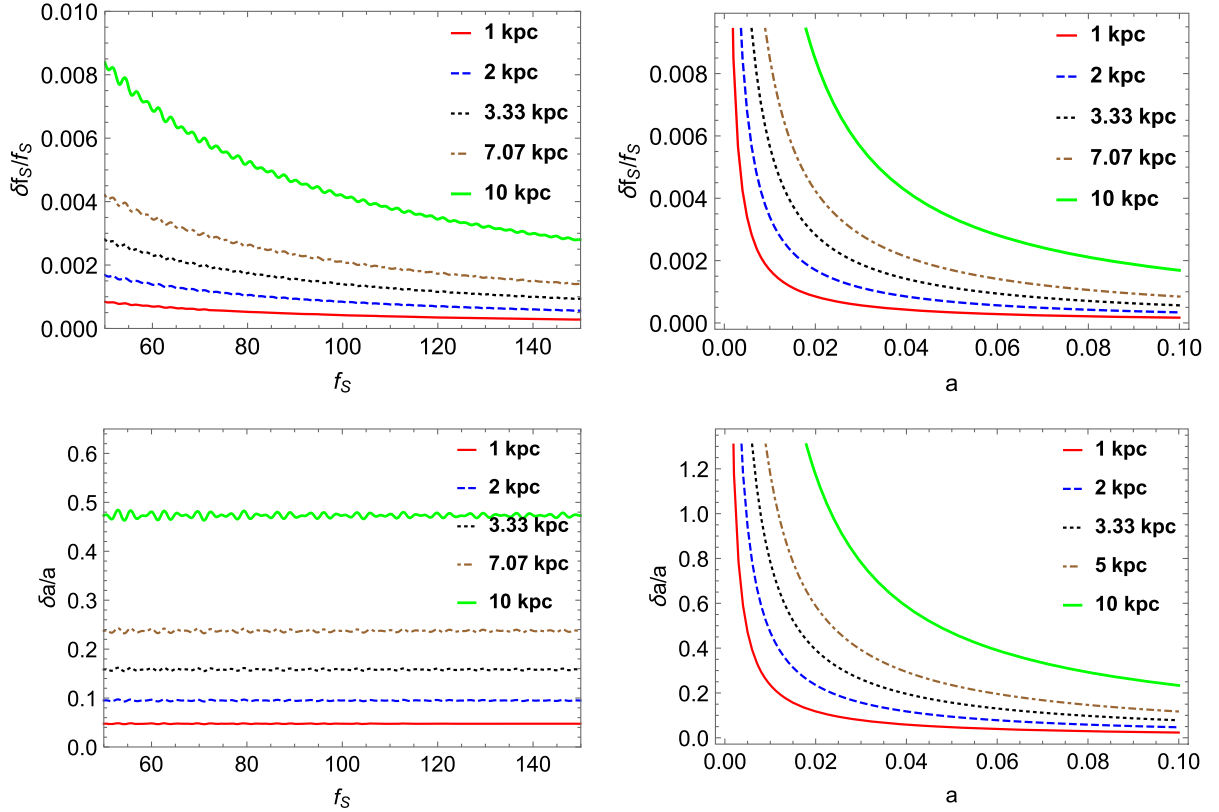
and

FIG. 6. Cramer-Rao lower bounds based on simplified parametric templates with SASI [see Eq. (1)], in the form of relative errors, for the SASI frequency (top) and amplitude (bottom), as functions of frequency (left) and amplitude (right), for Hyper-K and select distances to the star (see legend). In each curve, the remaining parameter has been fixed at its best-estimated value (the one for $D = 1$ kpc) in Table I.

$$\Gamma_{22} = \sum_{i=1}^{N} \frac{4a^2(A-n)^2\pi^2 t_i^2 \cos{(2\pi f_s t_i)}^2}{(A-n)(1+a\sin{(2\pi f_s t_i)})+n}$$
$$+ \frac{2a^2(A-n)^2\pi^2 t_i^2 \cos{(2\pi f_s t_i)}^2}{((A-n)(1+a\sin{(2\pi f_s t_i)})+n)^2}. \quad (27)$$

Finally, by combining Eqs. (24)–(27) with Eq. (20), one finds the minimum uncertainties on the parameters: $\delta\theta_1 = \delta a$ and $\delta\theta_2 = \delta f_S$. These are themselves functions of a and f_S, so they have to be estimated at a chosen (best-fit) point in the parameter space.

In Figs. 6 and 7, the relative Cramer-Rao uncertainties are shown for selected distances to the star (which determine the widths of the Gaussian probability distributions that enter the calculation), and as functions of one of the parameters, where the other parameter is kept fixed at its best-estimated value (last columns of Tables I and II). As expected, the uncertainties decrease with decreasing distance. We also note that the dependence on the amplitude a is stronger than that on the frequency.

As a figure of merit, to clarify if our approach is optimal we can compare the width (error) from the histograms in Fig. 5 with the Cramer-Rao lower bound for the SASI analytical model we adopt. In Tables I and II the

Cramer-Rao uncertainties—calculated at the points in the parameter space given in the tables themselves—are listed for the two smallest distances. They can be directly compared to the standard deviations obtained with the likelihood ratio method, because at such distances the selection effects due to the threshold on $\mathcal{L}$ are negligible (nearly all the simulated cases pass the selection). For larger D, where the selection effects on $\mathcal{L}$ are strong, a direct comparison is not meaningful and therefore the Cramer-Rao bounds are not shown.

It appears that δa obtained from the likelihood ratio is close (slightly larger, as expected) to the corresponding Cramer-Rao bound, indicating that our method is near optimality for estimating the SASI amplitude. In contrast, for δf_S the Cramer-Rao bound is orders of magnitude more stringent, so in principle, a more effective method than ours for frequency estimation could exist (although an estimator attaining the Cramer-Rao lower bound does not necessarily exist).

V. SUMMARY AND DISCUSSION

We have proposed a novel methodology to do both hypothesis testing and parameter estimation for signatures of SASI in the time profile of the neutrino event rate from a
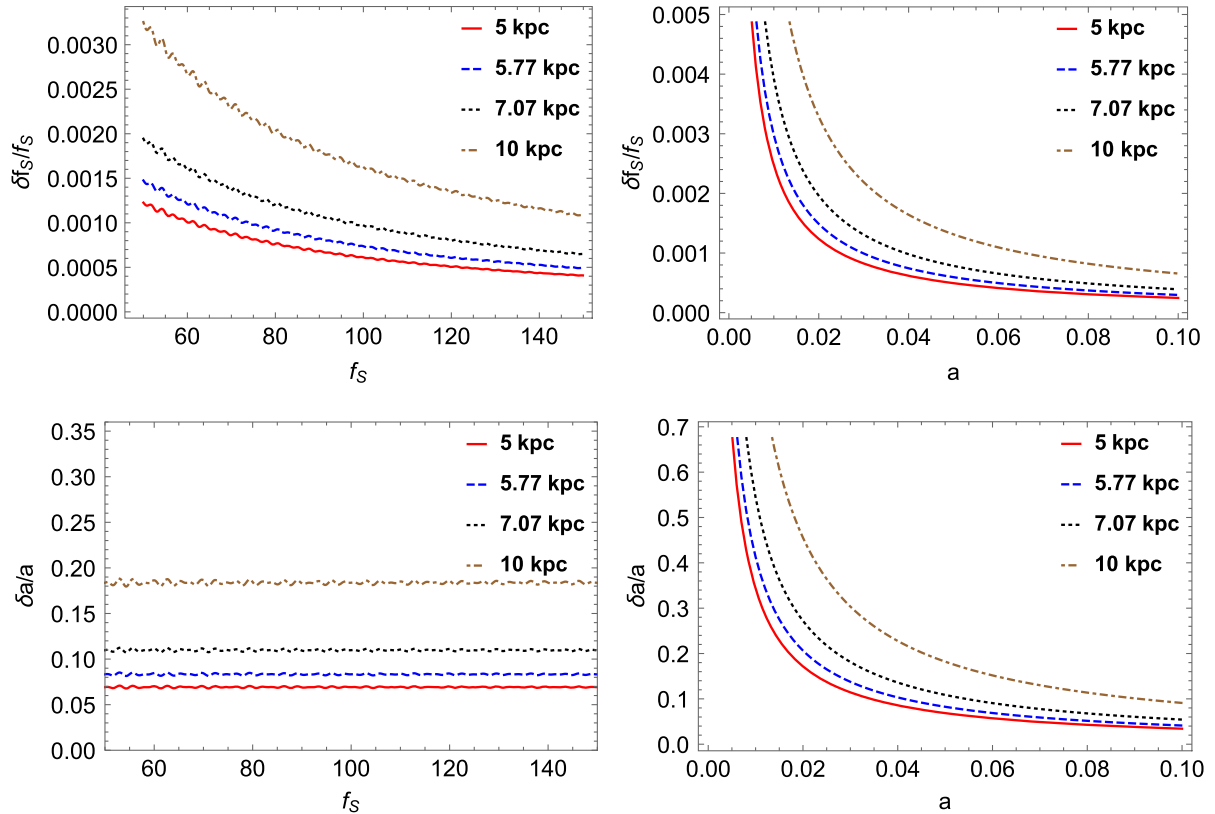

FIG. 7.   Cramer-Rao lower bounds based on simplified parametric templates with SASI [see Eq. (1)], in the form of relative errors, for the SASI frequency (top) and amplitude (bottom), as functions of frequency (left) and amplitude (right), for IceCube and select distances to the star (see legend). In each curve, the remaining parameter has been fixed at its best-estimated value (the one for $D = 1$ kpc) in Table II.

(galactic) core collapse supernova. This method is based on the likelihood ratio constructed using the signal power spectrum, for which the effect of statistical fluctuations was modeled, and suitable frequency cuts can be applied. We quantify the confidence to identify the presence of SASI in terms of receiver operating curves, a tool which is commonly used in the gravitational wave community to establish the efficiency versus false alarm probability for gravitational wave signals (see, e.g., [51]). We have tested the effectiveness of the method, using an injected signal for Hyper-K and IceCube from a supernova numerical simulation by Kuroda, Kotake, Hayama, and Takiwaki. Specifically, we have characterized the performance of the method by producing the receiver operating characteristic curves, and by comparing the probability distributions of the best fit parameters (the SASI frequency and relative amplitude) with the ultimate minimum uncertainties from the Cramer-Rao lower bounds.

For hypothesis testing, our main result are the probability distributions in Fig. 3. Figuratively speaking, these can be considered like a calibrated measurement rod against which we will compare the likelihood ratio from an actual, future supernova neutrinos detection. We have found that, for a nearby supernova, this "SASI-meter" is an effective tool: if the experimental likelihood ratio is in the "red zone" (above a certain threshold for the likelihood ratio, e.g., $\ln \mathcal{L} \gtrsim 30$ for Hyper-K and $D \simeq 2$ kpc), then we will be able to confidently claim the presence of SASI. If it is in the "blue zone" ($\ln \mathcal{L} \lesssim 20$ in the same example), then a model without SASI will be favored, and an upper bound on the parameters of possible SASI will be established. We obtain that, for the KKHT model, SASI can be identified with high confidence for a distance to the supernova of up to ~6 kpc for IceCube and up to ~3 kpc for Hyper-K. The SASI-meter can also be used to identify unusually long periods of SASI, which could help to establish indication of a failed supernova.

For parameter estimation, we find that, for an injected signal with SASI and for datasets in the red zone of the SASI-meter, the SASI frequency and amplitude can be reconstructed if $D \lesssim 5$ kpc for Hyper-K ($D \lesssim 10$ kpc for IceCube), and their uncertainties are consistent with the Cramer-Rao lower bounds. Beyond such distance, the positive response of the SASI-meter, giving indication of an oscillatory pattern in the event rate, is to be attributed to statistical fluctuations and not to the presence of SASI. The most immediate development of this work will include several three-dimensional supernova simulation results that present SASI and map the performance of the method in different regions of the parameter space. We expect that including several models will result in a blurring of the probability distributions, so the red and blue zones of the SASI-meter will be less clearly separated, or, in other words, the receiver operating characteristic curves will be worse (i.e., closer to the limiting curve $P_D = P_{\text{FI}}$). The method will remain valid conceptually, however.

In the long term, our goal is to extend the methodology to joint analyses of neutrino and gravitational wave SASI signals, for a truly multimessenger approach [52–54]. Within this goal, the present paper serves to create the foundation of a formalism for neutrinos that finds a direct counterpart (using the same tools, like the likelihood ratio and the receiver operating characteristic curve, for example) in existing gravitational wave analysis protocols. Moving forward, new approaches will have to be developed to establish how to most effectively combine the two signals, neutrinos and gravitational waves, that have both similarities (e.g., similar SASI frequency) and important differences (different sources of noise, for example). Such development work will explore further the territory of multimessenger astronomy and aid the investigation of a future galactic core collapse supernova.

ACKNOWLEDGMENTS

APPENDIX A: PROBABILITY DISTRIBUTION OF FOURIER TRANSFORMED NEUTRINO SIGNAL

In this Appendix the probability distribution of a Fourier transformed neutrino signal in frequency domain defined in Eq. (6) is given. We start from the real part of $\tilde{h}$:

$$\text{Re}(\tilde{h}) = \sum_{j=0}^{N_{\text{bins}}-1} \tilde{N}(t_j) \cos(2\pi t_j k\delta), \qquad (A1)$$

where $\tilde{N}$ is the observed event number in a time bin, statistically fluctuating around its mean value N.

To simplify the notation, let us define $\tilde{N}_j \equiv \tilde{N}(t_j)$, $\tilde{n}_j \equiv \tilde{N}_j \cos(2\pi t_j k\delta)$, and $\tilde{h}_R \equiv \text{Re}(\tilde{h})$. Here n_j and N_j will be means of $\tilde{n}_j$ and $\tilde{N}_j$ respectively, so that $n_j = N_j \cos(2\pi t_j k\delta)$. Since the neutrino event number $\tilde{N}_j = \tilde{R}(t_j)\Delta$ follows a Gaussian distribution (with variance $\sqrt{N_j}$), $\tilde{n}_j$ also follows a Gaussian distribution, with variance $\sqrt{N_j} \cos(2\pi t_j k\delta)$. Specifically, the two distributions are

$$\text{Prob}(\tilde{N}_j) = \frac{1}{\sqrt{2\pi N_j}} e^{-\frac{(\tilde{N}_j - N_j)^2}{2N_j}}, \qquad (A2)$$

$$\text{Prob}(\tilde{n}_j) = \frac{1}{\sqrt{2\pi N_j \cos^2(2\pi t_j k\delta)}} e^{-\frac{(\tilde{n}_j - n_j)^2}{2N_j \cos^2(2\pi t_j k\delta)}}. \qquad (A3)$$

Below we show that the Fourier transformed neutrino signal in frequency domain, which is a sum of Gaussian distributed random values, follows a Gaussian distribution as well. The probability distribution for $\tilde{h}_R$ is defined as:

$$\text{Prob}(\tilde{h}_R) = \int \left(\prod_{j=0}^{N_{\text{bins}}-1} \text{Prob}(\tilde{n}_j) \right) \delta \left(\tilde{h}_R - \sum_{j=0}^{N_{\text{bins}}-1} \tilde{n}_j \right)$$
$$\times d\tilde{n}_0 \ldots d\tilde{n}_j. \qquad (A4)$$

Let us now perform a Fourier transform of Eq. (A4):

$$\int \text{Prob}(\tilde{h}_R) e^{il\tilde{h}_R} d\tilde{h}_R = \int \left(\prod_{j=0}^{N_{\text{bins}}-1} \text{Prob}(\tilde{n}_j) \right)$$
$$\times e^{il \sum_{j=0}^{N_{\text{bins}}-1} \tilde{n}_j} d\tilde{n}_0 \ldots d\tilde{n}_j$$
$$= \prod_{j=0}^{N_{\text{bins}}-1} \int \text{Prob}(\tilde{n}_j) e^{il\tilde{n}_j} d\tilde{n}_j, \qquad (A5)$$

and note that the Fourier transform of a Gaussian distribution $P_G(x)$ with mean value μ and standard deviation σ is

$$\int P_G(x) e^{ilx} dx = e^{il\mu} e^{-\frac{\sigma^2 l^2}{2}}. \qquad (A6)$$

Then, we get:

$$\int \text{Prob}(\tilde{h}_R) e^{il\tilde{h}_R} d\tilde{h}_R = e^{il \sum_{j=0}^{N_{\text{bins}}-1} n_j}$$
$$\times e^{-l^2 \frac{\sum_{j=0}^{N_{\text{bins}}-1} n_j^2}{2N_j}}. \qquad (A7)$$

We then do an inverse Fourier transformation of Eq. (A7), and obtain:

$$\text{Prob}(\tilde{h}_R) = \frac{1}{\sqrt{2\pi \sum_{j=0}^{N_{\text{bins}}-1} N_j \cos^2(2\pi t_j k\delta)}}$$
$$\times e^{\frac{-(\tilde{h}_R - \sum_{j=0}^{N_{\text{bins}}-1} n_j)^2}{2 \sum_{j=0}^{N_{\text{bins}}-1} N_j \cos^2(2\pi t_j k\delta)}}$$
$$= \frac{1}{\sqrt{2\pi \sigma_R^2}} e^{\frac{(\tilde{h}_R - h_R)}{2\sigma_R^2}}, \qquad (A8)$$

with $\sigma_R^2 = \sum_{j=0}^{N_{\text{bins}}-1} N_j \cos^2(2\pi t_j k\delta)$ and $h_R = \sum_{j=0}^{N_{\text{bins}}-1} n_j$.

Equation (A8) concludes the proof for the real part of $\tilde{h}$. A similar proof can be done for the imaginary part of $\tilde{h}$, with the replacement $\cos(2\pi t_j k\delta) \rightarrow \sin(2\pi t_j k\delta)$, leading to a result analogous to Eq. (A8).

Let us now prove the statistical independence of the values of $\tilde{h}$ in different frequency bins. First, it is known that neutrino event rates in each time bin are statistically independent, i.e.:

$$\langle \tilde{N}(t_1) \tilde{N}(t_2) \rangle = \langle \tilde{N}(t_1) \rangle \langle \tilde{N}(t_2) \rangle, \qquad (A9)$$

where $t_1 \neq t_2$. It then follows that:

$$\langle \tilde{h}(k\delta) \tilde{h}^*(k'\delta) \rangle = \sum_{m}^{N_{\text{bins}}} \sum_{l}^{N_{\text{bins}}} e^{it_l k\delta} \langle \tilde{N}(t_l) \tilde{N}(t_m) \rangle e^{-it_m k'\delta}$$
$$= \sum_{l}^{N_{\text{bins}}} e^{it_l k\delta} \langle \tilde{N}(t_l) \rangle \sum_{m}^{N_{\text{bins}}} \langle \tilde{N}(t_m) \rangle e^{-it_m k'\delta}$$
$$+ \sum_{l}^{N_{\text{bins}}} N(t_l) e^{-it_l(k-k')\delta}$$
$$= \langle \tilde{h}(k\delta) \rangle \langle \tilde{h}^*(k'\delta) \rangle + \sum_{l}^{N_{\text{bins}}} N(t_l) e^{-it_l(k-k')\delta}. \qquad (A10)$$

The second term on the right-hand side of Eq. (A10) comes from the contribution of the terms with $l = m$, and is much smaller than the first term given that $N \gg 10$ and $N_{\text{bins}} \gg 10$. Therefore, Eq. (A10) shows an approximate statistical independence for $\tilde{h}$ in different frequency bins. The same conclusion can be reached for the real and imaginary parts of $\tilde{h}$ ($\tilde{h} = h_R + ih_I$) by rewriting Eq. (A10) in terms of h_R and h_I.

APPENDIX B: PROBABILITY DISTRIBUTION OF POWER

In this Appendix we derive Eq. (8). The power at a specific frequency is written as:

$$\tilde{P} = C(\tilde{h}_R^2 + \tilde{h}_I^2), \qquad (B1)$$

where $C = 2/N_{\text{bins}}^2$ is the normalization factor from Eq. (7). It can be shown that the standard deviations of $\tilde{h}_R$ and $\tilde{h}_I$, denoted as σ_R^2 and σ_I^2 respectively, are approximately equal, with differences of less than 10% (we checked this by comparing the two quantities in the whole space of the parameters $\Omega = \{a, f_S\}$). Accordingly in the following we assume that:

$$\sigma_R^2 \approx \sigma_I^2 \approx \sigma^2 \equiv \frac{\sigma_I^2 + \sigma_R^2}{2}$$

$$= \sum_{j=0}^{N_{\text{bins}}-1} \frac{N_j(\cos^2(2\pi t_j k\delta) + \sin^2(2\pi t_j k\delta))}{2}$$

$$= \frac{N_{ev}}{2}. \tag{B2}$$

We now define new variable $\tilde{P}'$:

$$\tilde{P}' = \frac{\tilde{P}}{C\sigma^2} = \frac{\tilde{h}_R^2 + \tilde{h}_I^2}{\sigma^2}. \tag{B3}$$

Note that both $\tilde{h}_R/\sigma$ and $\tilde{h}_I/\sigma$ are Gaussian random variables with unit standard deviation given Eq. (B2). As a result, $\tilde{P}'$ follows a noncentral-chi-squared distribution [41]:

$$\text{Prob}(\tilde{P}') = \frac{1}{2} e^{\frac{1}{2}(\tilde{P}'+\lambda')} I_0(\sqrt{\lambda'\tilde{P}'}), \tag{B4}$$

where $\lambda' = (h_R^2 + h_I^2)/\sigma^2$ is the noncentrality parameter and I_0 is the modified Bessel function of the first kind. By using the normalization condition:

$$\int \text{Prob}(\tilde{P}')d\tilde{P}' = \int \text{Prob}(\tilde{P})d\tilde{P} = 1, \tag{B5}$$

the probability density function of $\tilde{P}$ is

$$\text{Prob}(\tilde{P}) = \frac{1}{2} e^{-\frac{1}{2}(\frac{\tilde{P}}{C\sigma^2}+\lambda')} I_0\left(\sqrt{\lambda'\frac{\tilde{P}}{C\sigma^2}}\right) \frac{1}{C\sigma^2}. \tag{B6}$$

We then insert Eqs. (B1) and (B2) into Eq. (B6) to get the probability density function as written in Eq. (8). The

analytical expression for the probability density distribution of power agrees very well with our numerical Monte Carlo simulation.

APPENDIX C: FISHER MATRIX

In this Appendix, we show that Eq. (16) follows from Eq. (15).

Integrating by parts with null boundary condition, Eq. (15) can be re-written as:

$$\Gamma_{\alpha\beta} = \int -\frac{\partial^2 \ln \text{Prob}(\tilde{R})}{\partial\theta_\alpha\theta_\beta} \text{Prob}(\tilde{R}) d\tilde{R}$$

$$= \int \frac{\partial \ln \text{Prob}(\tilde{R})}{\partial\theta_\alpha} \frac{\partial \ln \text{Prob}(\tilde{R})}{\partial\theta_\beta} \text{Prob}(\tilde{R}) d\tilde{R}. \tag{C1}$$

Using the expression:

$$\ln \text{Prob}(\tilde{R}) = \sum_i \left(-\frac{1}{2}\ln(2\pi\sigma_i^2) - \frac{(\tilde{R}_i - R_i)^2}{2\sigma_i^2}\right), \tag{C2}$$

we then obtain:

$$\frac{\partial \ln \text{Prob}(\tilde{R})}{\partial\theta_\alpha} = \sum_i \frac{1}{\sigma_i^2}(\tilde{R}_i - R_i)\frac{\partial R_i}{\partial\theta_\alpha}$$

$$+ \sum_i \left(-\frac{1}{2\sigma_i^2}\frac{\partial\sigma_i^2}{\partial\theta_\alpha} + \frac{(\tilde{R}_i - R_i)^2}{2\sigma_i^4}\left(\frac{\partial\sigma_i^2}{\partial\theta_\alpha}\right)\right). \tag{C3}$$

The integration in Eq. (C1) is then divided into several parts, and becomes:

$$\int \frac{\partial \ln \text{Prob}(\tilde{R})}{\partial\theta_\alpha}\frac{\partial \ln \text{Prob}(\tilde{R})}{\partial\theta_\beta}\text{Prob}(\tilde{R})d\tilde{R} = \sum_i \frac{\partial R_i}{\partial\theta_\alpha}\frac{\partial R_j}{\partial\theta_\beta}\frac{1}{\sigma_i^2} + \sum_{i,j}\left(\frac{1}{2\sigma_i^2}\frac{\partial\sigma_i^2}{\partial\theta_\alpha}\right)\left(\frac{1}{2\sigma_j^2}\frac{\partial\sigma_j^2}{\partial\theta_\beta}\right)$$

$$+ \int d\tilde{R}\sum_{i,j}\frac{(\tilde{R}_i - R_i)^2}{2\sigma_i^4}\frac{\partial\sigma_i^2}{\partial\theta_\alpha}\frac{(\tilde{R}_j - R_j)^2}{2\sigma_j^4}\frac{\partial\sigma_j^2}{\partial\theta_\beta}\text{Prob}(\tilde{R})$$

$$+ \int d\tilde{R}\sum_{i,j}\left(-\frac{1}{2\sigma_i^2}\frac{\partial\sigma_i^2}{\partial\theta_\alpha}\right)\frac{(\tilde{R}_j - R_j)^2}{2\sigma_j^4}\frac{\partial\sigma_j^2}{\partial\theta_\beta}\text{Prob}(\tilde{R}) + \{i \leftrightarrow j\}. \tag{C4}$$

Note that:

$$\langle(\tilde{R} - R)^4\rangle = 3\sigma^4, \tag{C5}$$

and that the second and the fourth term in Eq. (C4) sum to zero. Finally Eq. (C4) becomes:

$$\Gamma_{\alpha\beta} = \sum_i \frac{\partial R_i}{\partial\theta_\alpha}\frac{\partial R_j}{\partial\theta_\beta}\frac{1}{\sigma_i^2} + \frac{1}{2}\sum_i \frac{1}{\sigma_i^2}\frac{\partial\sigma_i^2}{\partial\theta_\alpha}\frac{1}{\sigma_i^2}\frac{\partial\sigma_i^2}{\partial\theta_\theta}$$

$$= \mu_\alpha^T \Sigma^{-1}\mu_\beta + \frac{1}{2}\text{Tr}[\tilde{c}_\alpha\tilde{c}_\beta], \tag{C6}$$

which concludes the proof.

[1] J. M. Blondin, A. Mezzacappa, and C. DeMarino, Astrophys. J. **584,** 971 (2003).

[2] T. Foglizzo et al., Pub. Astron. Soc. Aust. **32,** e009 (2015).

[3] A. Mirizzi, I. Tamborra, H.-T. Janka, N. Saviano, K. Scholberg, R. Bollig, L. Hudepohl, and S. Chakraborty, Riv. Nuovo Cimento **39,** 1 (2016).

[4] T. Kuroda, K. Kotake, K. Hayama, and T. Takiwaki, Astrophys. J. **851,** 62 (2017).

[5] H. Andresen, B. Mller, E. Mller, and H.-T. Janka, Mon. Not. R. Astron. Soc. **468,** 2032 (2017).

[6] B. Müller and H.-T. Janka, Astrophys. J. **788,** 82 (2014).

[7] J. M. Blondin and S. Shaw, Astrophys. J. **656,** 366 (2007).

[8] A. Marek, H. T. Janka, and E. Mueller, Astron. Astrophys. **496,** 475 (2009).

[9] A. Marek and H. T. Janka, Astrophys. J. **694,** 664 (2009).

[10] K. Nakamura, T. Takiwaki, T. Kuroda, and K. Kotake, Publ. Astron. Soc. Jpn. **67,** 107 (2015).

[11] A. Summa, F. Hanke, H.-T. Janka, T. Melson, A. Marek, and B. Mller, Astrophys. J. **825,** 6 (2016).

[12] J. M. Blondin and A. Mezzacappa, Nature (London) **445,** 58 (2007).

[13] W. Iwakami, K. Kotake, N. Ohnishi, S. Yamada, and K. Sawada, Astrophys. J. **700,** 232 (2009).

[14] R. Fernandez, Astrophys. J. **725,** 1563 (2010).

[15] F. Hanke, B. Mueller, A. Wongwathanarat, A. Marek, and H.-T. Janka, Astrophys. J. **770,** 66 (2013).

[16] E. P. O'Connor and S. M. Couch, Astrophys. J. **865,** 81 (2018).

[17] D. Vartanyan, A. Burrows, and D. Radice, Mon. Not. R. Astron. Soc. **489,** 2227 (2019).

[18] L. Walk, I. Tamborra, H.-T. Janka, and A. Summa, Phys. Rev. D **101,** 123013 (2020).

[19] I. Tamborra, F. Hanke, B. Müller, H.-T. Janka, and G. Raffelt, Phys. Rev. Lett. **111,** 121104 (2013).

[20] L. Walk, I. Tamborra, H.-T. Janka, and A. Summa, Phys. Rev. D **98,** 123001 (2018).

[21] T. Lund, A. Marek, C. Lunardini, H.-T. Janka, and G. Raffelt, Phys. Rev. D **82,** 063007 (2010).

[22] J. F. Beacom and P. Vogel, Phys. Rev. D **58,** 093012 (1998).

[23] M. Rampp and H. T. Janka, Astron. Astrophys. **396,** 361 (2002).

[24] R. Buras, M. Rampp, H. T. Janka, and K. Kifonidis, Astron. Astrophys. **447,** 1049 (2006).

[25] B. Mueller, H.-T. Janka, and A. Marek, Astrophys. J. **766,** 43 (2013).

[26] T. Lund, A. Wongwathanarat, H.-T. Janka, E. Muller, and G. Raffelt, Phys. Rev. D **86,** 105031 (2012).

[27] J. Migenda, Ph.D. thesis, Max Planck Institute, 2016.

[28] I. Tamborra, F. Hanke, H.-T. Janka, B. Mller, G. G. Raffelt, and A. Marek, Astrophys. J. **792,** 96 (2014).

[29] K. Abe et al. (Hyper-Kamiokande Collaboration), arXiv:1805.04163.

[30] K. Scholberg, Annu. Rev. Nucl. Part. Sci. **62,** 81 (2012).

[31] L. Köpke (IceCube Collaboration), J. Phys. Conf. Ser. **1029,** 012001 (2018).

[32] T. Kowarik, T. Griesel, and A. Piegsa (IceCube Collaboration), arXiv:0908.0441.

[33] A. W. Steiner, M. Hempel, and T. Fischer, Astrophys. J. **774,** 17 (2013).

[34] S. E. Woosley and T. A. Weaver, Astrophys. J. Suppl. Ser. **101,** 181 (1995).

[35] K. N. Yakunin, A. Mezzacappa, P. Marronetti, E. J. Lentz, S. W. Bruenn, W. R. Hix, O. E. Bronson Messer, E. Endeve, J. M. Blondin, and J. A. Harris, arXiv:1701.07325.

[36] T. Kuroda, K. Kotake, and T. Takiwaki, Astrophys. J. **829,** L14 (2016).

[37] M. Shibata and T. Nakamura, Phys. Rev. D **52,** 5428 (1995).

[38] T. W. Baumgarte and S. L. Shapiro, Phys. Rev. D **59,** 024007 (1998).

[39] T. Kuroda, K. Kotake, and T. Takiwaki, Astrophys. J. **755,** 11 (2012).

[40] S. P. Mikheyev and A. Yu. Smirnov, Sov. J. Nucl. Phys. **42,** 913 (1985).

[41] S. M. Kay, Fundamentals of Statistical Processing, Volume 2: Detection Theory, Prentice-Hall Signal Processing Series (Pearson Education, New Jersey, 2009).

[42] D. Radice, V. Morozova, A. Burrows, D. Vartanyan, and H. Nagakura, Astrophys. J. **876,** L9 (2019).

[43] J. Powell and B. Mller, Mon. Not. R. Astron. Soc. **487,** 1178 (2019).

[44] E. Müller, H. T. Janka, and A. Wongwathanarat, Astron. Astrophys. **537,** A63 (2012).

[45] Equation (3) implies that a that much longer SASI signature will result in more precise estimation of the frequency; this might be relevant for future work on long-stalling shock-waves.

[46] E. Mueller, M. Rampp, R. Buras, H. T. Janka, and D. H. Shoemaker, Astrophys. J. **603,** 221 (2004).

[47] J. W. Murphy, C. D. Ott, and A. Burrows, Astrophys. J. **707,** 1173 (2009).

[48] K. N. Yakunin et al., Classical Quantum Gravity **27,** 194005 (2010).

[49] Note that, all cases, the logarithm of the likelihood ratio is positive, meaning that the two parameter template offers a better fit than the zero-parameters one. This is simply a consequence of the larger number of parameters of one template with respect to the other.

[50] For very high statistics signals, an accurate evaluation of the parameter distributions will require a finer sampling of the parameter space than done here. We checked that the effect of the finite sampling is minor in our results.

[51] L. Blackburn et al., Classical Quantum Gravity **22,** S1293 (2005).

[52] M. G. Aartsen et al. (IceCube, Fermi-LAT, MAGIC, AGILE, ASAS-SN, HAWC, H.E.S.S., INTEGRAL, Kanata, Kiso, Kapteyn, Liverpool Telescope, Subaru, Swift NuSTAR, VERITAS, and VLA/17B-403 Collaboration), Science **361,** eaat1378 (2018).

[53] M. Branchesi, J. Phys. Conf. Ser. **718,** 022004 (2016).

[54] V. Kalogera et al., arXiv:1903.09224.